Scientific Research Publishing

Advances in Nanoparticles, 2026, 15(2), 37-57
https://www.scirp.org/journal/anp
ISSN Online: 2169-0529
ISSN Print: 2169-0510

Microstructural Study of a Cerium-Based Metal-Organic Framework Compound by Analysis of X-Ray Diffraction Peak Broadening

Ferland Ngoro-Elenga[1,2*], Hubert Makomo[3], Fernand Atipo Itoua Ngopoh[1], Coeursa Aurore Leko[1], Arnaud Ottard Ossiby Mwa Ngo[1], Timothée Nsongo[2]

[1]Laboratory of Inorganic and Applied Chemistry, Marien Ngouabi University, Brazzaville, Congo
[2]Geological and Mining Research Center, Ministry of Mining Industries and Geology, Brazzaville, Congo
[3]Laboratory of Organic Chemistry, Marien Ngouabi University, Brazzaville, Congo
Email: *ferland.ngoro-elenga@umng.cg

How to cite this paper: Ngoro-Elenga, F., Makomo, H., Ngopoh, F.A.I., Leko, C.A., Ngo, A.O.O.M. and Nsongo, T. (2026) Microstructural Study of a Cerium-Based Metal-Organic Framework Compound by Analysis of X-Ray Diffraction Peak Broadening. *Advances in Nanoparticles*, **15**, 37-57.
https://doi.org/10.4236/anp.2026.152002

Received: March 10, 2026
Accepted: May 28, 2026
Published: May 31, 2026

Abstract

The microstructural characterization of cerium-based metal-organic frameworks (Ce-MOF) is essential for understanding the relationship between crystal structure and functional properties. In this study, the synthesized Ce-MOF was characterized by powder X-ray diffraction (PXRD), scanning electron microscopy coupled with energy-dispersive X-ray spectroscopy (SEM-EDS), Fourier-transform infrared spectroscopy (FTIR), and X-ray fluorescence (XRF). X-ray diffraction peak broadening was analyzed to separate the contributions of coherent diffraction domain size and lattice microstrain. A comparative analysis was performed using the Scherrer (53.91 nm), Monshi-Scherrer (49.79 nm), Williamson-Hall (47.00 nm; $\varepsilon = 2.585 \times 10^{-4}$), Size-Strain Plot (42.27 nm; $\varepsilon = 6.614 \times 10^{-4}$), Halder-Wagner (42.27 nm; $\varepsilon = 1.073 \times 10^{-3}$), and modified Warren-Averbach (46.97 nm; $\varepsilon = 8.587 \times 10^{-4}$) methods. The strain-inclusive models converged toward a consistent description of the microstructure, indicating coherent diffraction domains ranging from 42 to 54 nm and lattice microstrains on the 10^{-4} - 10^{-3}. The relatively small variation in the estimated coherent domain sizes suggests that the diffraction peak broadening is predominantly governed by the finite size of the coherent domains, whereas the contribution of the lattice microstrain remains comparatively limited. SEM observations revealed irregularly shaped particles with heterogeneous size distribution. FTIR spectra exhibited the characteristic vibration bands associated with Ce-O coordination, confirming the successful formation of the Ce-MOF framework. The elemental composition determined by XRF and SEM-EDS further confirmed the successful formation of the constituent elements within the synthesized material.

Keywords

Ce-MOF, X-Ray Diffraction, Microstructure, Crystallite Size, Microstrain

1. Introduction

Metal-organic frameworks (MOFs)-based hybrid materials constitute an important class of porous crystalline solids. Their architecture results from the coordinated assembly of metal nodes and polydentate organic ligands, forming periodic networks [1]-[4]. The physicochemical properties of these materials are strongly dependent on the nature of the metal centers and the density of structural defects [5]-[7]. The structural modularity of MOFs, combined with their high specific surface area and the possibility of controlled functionalization of metal sites, endows them with tunable properties for applications in catalysis, separation, energy storage, and optics [8]-[10]. Cerium-based MOFs are of particular interest owing to the redox chemistry of cerium, which exhibits two oxidation states, +III and +IV, enabling the formation of highly connected oxo-cluster-type nodes [11] [12]. This redox duality, combined with the coordination flexibility of cerium, promotes oxygen vacancies [13] and local distortions. These phenomena make the structures highly dependent on synthesis conditions and lead to a complex microstructure, directly influencing crystallinity and defect density [14]-[16]. In this context, understanding the crystalline microstructure of Ce-MOFs is essential, particularly the determination of the size of coherent diffraction domains and lattice microstrain [17]-[19]. These parameters directly influence the structural stability, pore connectivity, and functional performance of MOFs [20] [21]. Powder X-ray diffraction is the reference tool for accessing this information, where the broadening of Bragg reflections simultaneously reflects the effects of finite coherent diffraction domain size and microstructural strain [22] [23]. The Scherrer approach provides an estimate of the average coherent diffraction domain size by assuming that peak broadening is purely dominated by coherent domain size. Several formalisms have been developed to better deconvolute microstructural contributions from diffraction profiles. The Monshi-Scherrer method proposes a linearized reformulation of the Scherrer equation, enabling a more stable estimation of coherent diffraction domain sizes. The Williamson-Hall approach allows the separation of size and microstrain contributions under the assumption of isotropic broadening [24] [25]. The Size-Strain Plot model provides an alternative weighting that reduces the influence of high-angle values [23], while the Halder-Wagner formalism relies on a pseudo-Voigt decomposition of size and strain contributions [24]. Finally, the Warren-Averbach approach enables a more rigorous analysis of peak broadening by separating microstructural contributions [26] [27], without explicit use of the Fourier transform in the present study. In this study, these different approaches were applied comparatively to a cerium-based MOF in order to evaluate the consistency of coherent diffraction domain sizes and lattice microstrain estimates.

The objective is to highlight the limitations of individual models in a highly heterogeneous system and to propose a cross-reading approach linking the observed microstrain to the nature of metal-ligand interactions and the redox chemistry of cerium. This comparative approach is essential for establishing structure-microstructure-function relationships in porous hybrid materials with high defect density or potentially defective character.

2. Experiment

2.1. Hydrothermal Synthesis of the Ce-MOF Material

In a beaker containing 50 mL of distilled water, 0.10 g of terephthalic acid (H_2BDC) was dispersed under magnetic stirring at room temperature for 15 minutes, yielding a solution of pH 6. A few drops of ammonia were then added to adjust the pH to 7. In a separate beaker, 0.17 g of ammoniacal cerium (IV) sulfate dihydrate was dissolved in 10 mL of distilled water under stirring at room temperature. The salt solution was gradually introduced into the H_2BDC acid solution at neutral pH. The resulting final solution was transferred into a 100 mL stainless steel autoclave lined with a Teflon insert and placed in an oven at 120˚C for 120 hours. The obtained powder was washed in a 50/50 mixture of distilled water and ethanol, then dried at room temperature for 24 hours.

2.2. Characterization Methods of the Synthesized Powder

Several techniques were employed to characterize the synthesized product. X-ray diffraction analysis was performed using a Bragg-Brentano geometry powder diffractometer (X'Pert3 Panalytical) equipped with a CuKα radiation source ($\lambda_{K\alpha 1}$ = 1.54059 Å; $\lambda_{K\alpha 2}$ = 1.54441 Å). Diffraction data were collected under the following experimental conditions: $5^\circ \leq 2\theta \leq 50^\circ$; $\Delta 2\theta = 0.02^\circ$; 45 kV; 100 mA. The microstructural parameters were estimated using the Scherrer, Monshi-Scherrer, Williamson-Hall, Halder-Wagner, Size-Strain Plot, and simplified Warren-Averbach methods. Only the diffraction peaks characteristic of the Ce-MOF phase was considered for the estimation of the microstructural parameters.

The morphology and elemental composition of the synthesized product were investigated by scanning electron microscopy coupled with energy-dispersive spectroscopy. Analyses were carried out using a Regulus SU 8100 microscope equipped with an energy-dispersive spectroscopy detector. SEM observations were performed at an accelerating voltage of 2 kV, with magnifications of ×100, ×500, ×1000, ×2000, and working distances of 7.9 mm and 8 mm. Elemental analysis by EDS was conducted at a magnification of ×3000, with an acquisition time of 7.68 µs, a real analysis time of 50 s, and an energy resolution of 123.8 eV.

The functional groups present in the synthesized product were identified by Fourier-transform infrared spectroscopy. Measurements were carried out using a Thermo Scientific Nicolet iS10 FTIR spectrometer. Spectra were recorded over the wavenumber range of 4000 - 400 cm^{-1}.

3. Results and Discussion

3.1. XRD Data Analysis

The XRD pattern of the synthesized compound (Figure 1) shows the appearance of characteristic peaks of Ce-MOF at approximately 2θ (˚) = 12.16; 15.62; 24.48; 25.16, with slight shifts relative to the literature [28] [29]. The absence of peaks at low angles (<10˚ 2θ) indicates a low degree of long-range crystallinity, suggesting that the synthesized compound exhibits either a nanocrystalline structure or a highly deficient MOF network. Several studies have shown that cerium-based MOFs can be amorphous or poorly crystalline, leading to the disappearance or broadening of low-angle peaks [18] [30]-[34] associated with pore periodicity. This structural disorder could be attributed to the sulfate precursors used in the synthesis, which would disrupt the formation of Ce-O clusters [35] [36]. The presence of an intense peak at 27.92˚ indicates the presence of CeO_2 as an impurity, confirmed by peaks at 33.3˚ and 47.56˚. The intense peak observed around 2θ = 17.3˚ may originate from the crystallization of unreacted or partially coordinated H_2BDC [30]. The angular positions and corrected FWHM values of the Ce-MOF diffraction peaks used to estimate the coherent diffraction domain size and lattice microstrain are listed in Table 1.

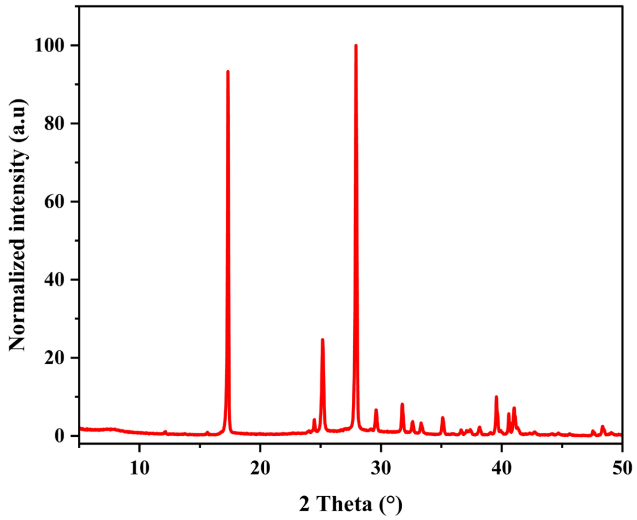

Figure 1. XRD pattern of the synthesized compound.

Table 1. Angular positions (2θ) and instrumental broadening-corrected full width at half maximum (FWHM, β).

2θ	24.48	25.17	29.59	31.77	32.62	35.12	38.16	39.58	40.59	41.04
β	0.132	0.186	0.188	0.156	0.153	0.143	0.117	0.166	0.137	0.211

3.2. Coherent Domain Sizes and Lattice Microstrain Estimation

3.2.1. Scherrer and Monschi-Scherrer Methods

The Scherrer method was used to rapidly estimate the average coherent diffraction domain sizes without accounting for the effects of lattice microstrain. Equation

(1) describes this method [37] [38]:

$$D = \frac{K \cdot \lambda}{\beta \cos\theta} \tag{1}$$

The Monshi-Scherrer (MS) method, also referred to as the modified Scherrer method, is derived from the logarithmic linearization of the Scherrer equation and is given by the following Equation (2) [39]:

$$\ln \beta = \ln\left(\frac{K \cdot \lambda}{D}\right) + \ln\left(\frac{1}{\cos\theta}\right) \tag{2}$$

With D: average coherent diffraction domain sizes (nm); K: Scherrer constant ($K = 0.9$); λ: X-ray wavelength (nm); β is the full width at half maximum (FWHM) after correction for instrumental broadening, in radians; θ is the Bragg angle in radians. The slope of the linear plot of ln β versus ln(1/cosθ) was used to determine the average coherent diffraction domain sizes. The Scherrer (Figure 2) and Monshi-Scherrer (Figure 3) methods yielded coherent diffraction domain sizes of 53.91 and 49.79 nm, respectively.

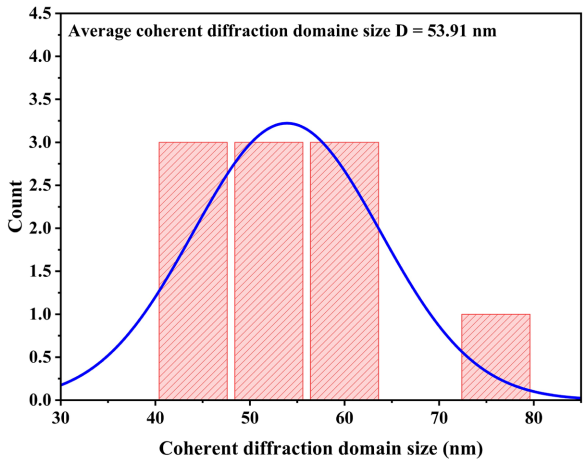

Figure 2. Scherrer method.

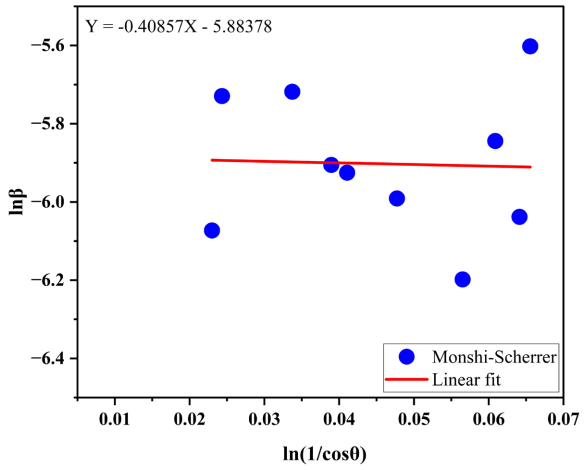

Figure 3. Monshi-Scherrer method.

3.2.2. Williamson-Hall Method

The Williamson-Hall (WH) method is one of the most widely used techniques for analyzing diffraction peak broadening, considering it as arising from the simultaneous contributions of coherent diffraction domain sizes and lattice microstrain, the latter resulting from point defects, grain boundaries, and stacking faults [40]-[42]. This broadening is defined by Equation (3):

$$\beta = \beta_{size} + \beta_{strain} \tag{3}$$

The Uniform Deformation Model (UDM) stipulates that the crystal deforms uniformly along all crystallographic directions, thereby causing isotropic peak broadening, and is expressed by Equation (4) [43] [44].

$$\beta\cos\theta = \frac{K\cdot\lambda}{D} + 4\varepsilon\sin\theta \tag{4}$$

where ε is the lattice microstrain. To exploit this relationship, a linear regression is performed by plotting $\beta\cos\theta$ as a function of $4\sin\theta$. Linear fitting of the experimental data (**Figure 4**) enabled the estimation of the microstructural parameters. The slope of the fitted line directly provided the lattice microstrain ($\varepsilon = 2.585 \times 10^{-4}$), whereas the intercept yielded a coherent diffraction domain size of 47.00. This approach therefore represents a simple and effective technique for evaluating microstructural parameters.

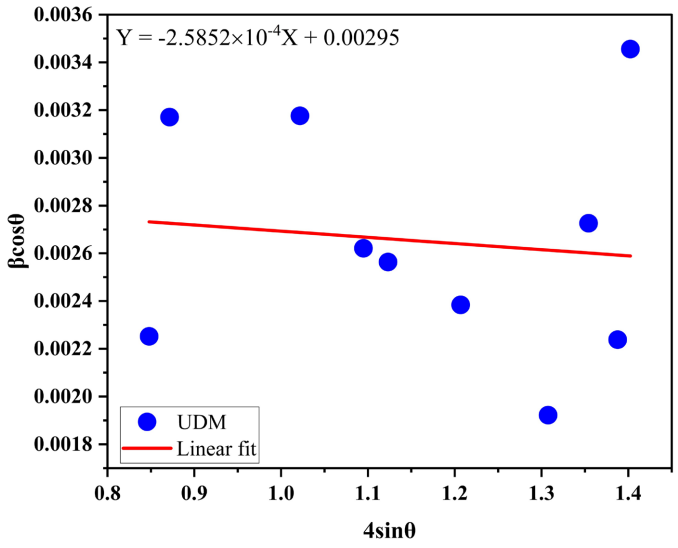

Figure 4. Williamson-Hall method.

3.2.3. Size-Strain Plot Method

In the Size-Strain Plot (SSP) approach, the broadening of diffraction peaks is considered as a combination of Lorentzian and Gaussian functions (Equation (5)), which are associated with coherent diffraction domain and microstrain, respectively [45]-[47].

$$\beta = \beta_L + \beta_G \tag{5}$$

where β_L and β_G are the full widths at half maximum of the Lorentzian and Gauss-

ian functions, respectively. The relationship is used to estimate the coherent diffraction domain sizes and lattice strain. Equation (6) [45] [47] estimates the coherent diffraction domain sizes and microstrain.

$$\left(d\cdot\beta\cdot\cos\theta\right)^2=\frac{K\cdot\lambda}{D}\left(d^2\cdot\beta\cdot\cos\theta\right)+\frac{\varepsilon^2}{4} \tag{6}$$

As shown in **Figure 5**, linear fitting of the $\left(d\cdot\beta\cdot\cos\theta\right)^2$ versus $\left(d^2\cdot\beta\cdot\cos\theta\right)$ plot provided a coherent diffraction domain size of 42.27 nm and a lattice microstrain of 6.614×10^{-4}, which was calculated from the slope and the intercept of the fitted line, respectively.

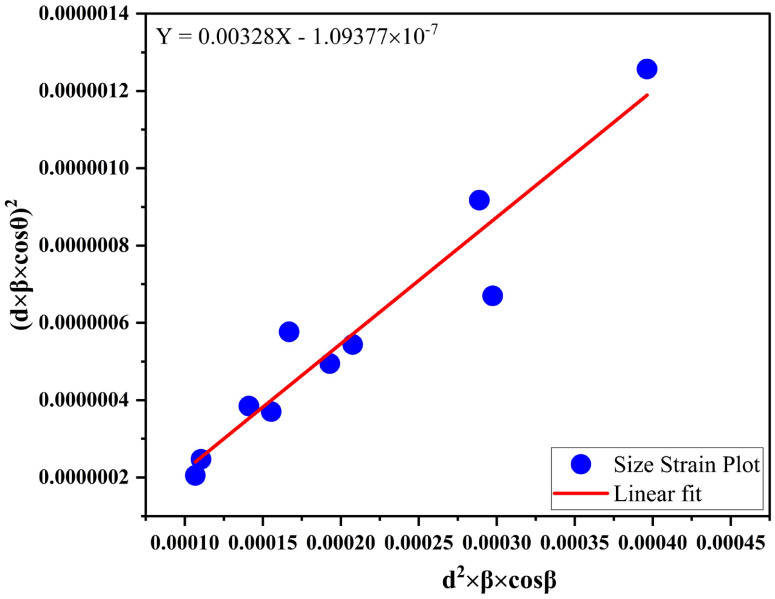

Figure 5. Size-strain plot method.

3.2.4. Halder-Wagner Method

The Halder-Wagner (HW) approach assumes that peak broadening follows a symmetric Voigt function, *i.e.*, a convolution of a Lorentzian and a Gaussian function [24] [38] [39] [48], and the observed full width at half maximum is given by Equation (7):

$$\beta^2=\beta_L\beta+\beta_G^2 \tag{7}$$

The relationship used to estimate these parameters using the Halder-Wagner method is given by Equation (8) [24] [39] [49]:

$$\left(\frac{\beta}{2\tan\theta}\right)^2=\frac{K\cdot\lambda}{D}\left(\frac{\beta}{4\tan\theta\cdot\sin\theta}\right)+4\varepsilon^2 \tag{8}$$

The linear regression of the $\left(\frac{\beta}{2\tan\theta}\right)^2$ versus $\left(\frac{\beta}{4\tan\theta\cdot\sin\theta}\right)$ plot (**Figure 6**) yielded a coherent diffraction domain size of 42.27 and a lattice microstrain of 1.073×10^{-3}, derived from the slope and the intercept of the fitted line, respectively.

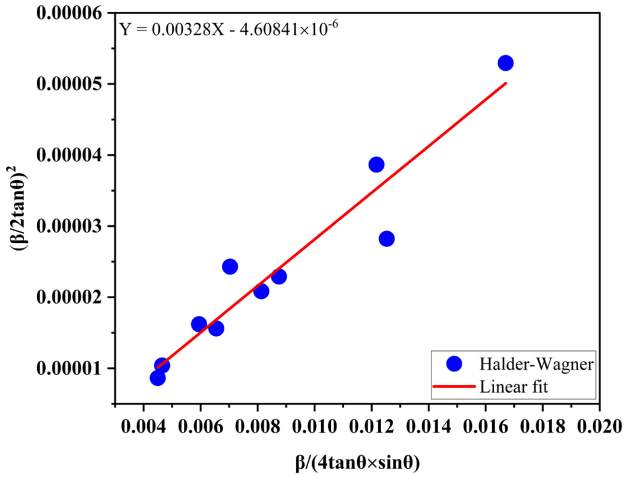

Figure 6. Halder-Wagner method.

3.2.5. Modified Warren-Averbach Method

The Warren-Averbach method is one of the diffraction profile analysis methods that allows the separation and quantification of crystallite size and internal lattice strain. The average dislocation density can also be obtained through this approach [50]-[53]. Given the complexity of applying the Warren-Averbach method, which requires the use of the Fourier transform, an equation inspired by this method but without the Fourier transform, expressed by Equation (9), has been proposed [54]-[56]:

$$\frac{\beta^2}{\tan^2\theta} = \frac{\lambda}{D}\left(\frac{\beta}{\tan\theta\sin\theta}\right) + 25\left\langle\varepsilon^2\right\rangle \tag{9}$$

Figure 7 presents the plot of $\frac{\beta^2}{\tan^2\theta}$ as a function of $\frac{\beta}{\tan\theta\sin\theta}$. Linear fitting of the experimental data yielded a coherent diffraction domain size of 46.97 nm and a lattice microstrain of 8.587×10^{-4}, obtained from the slope and the intercept of the fitted line, respectively.

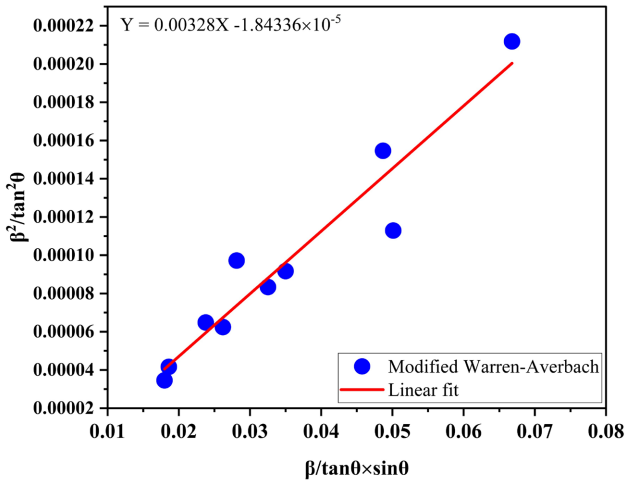

Figure 7. Modified Warren-Averbach method.

The microstructural analysis of the synthesized compound, performed through X-ray diffraction peak broadening, showed that the estimated coherent diffraction domain size and microstrain depend on the peak-broadening model employed (Figure 8). The estimated coherent diffraction domain size ranged from 42.27 to 53.91 nm, whereas the corresponding microstrain values varied between 2.585×10^{-4} and 1.703×10^{-3}. The Scherrer method yielded the largest coherent domain size (53.91 nm), whereas the size-strain plot and Halder-Wagner methods produced identical values of 42.27 nm. Intermediate values of 49.79, 47.00, and 46.96 nm were obtained using the Monshi-Scherrer, Williamson-Hall, and modified Warren-Averbach methods, respectively. This trend is consistent with the theoretical foundations of these approaches, which assign different contributions of crystallite size and lattice strain to diffraction peak broadening. The progressive decrease in the estimated coherent domain size from the Scherrer method to size-strain plot and Halder-Wagner models reflects the increasing consideration of the microstrain contribution to peak broadening. While the Scherrer equation attributes the entire peak broadening to the finite size of coherent diffraction domains, the Williamson-Hall, size-strain, and Halder-Wagner partition the observed broadening into contributions arising from finite domain size and lattice strain.

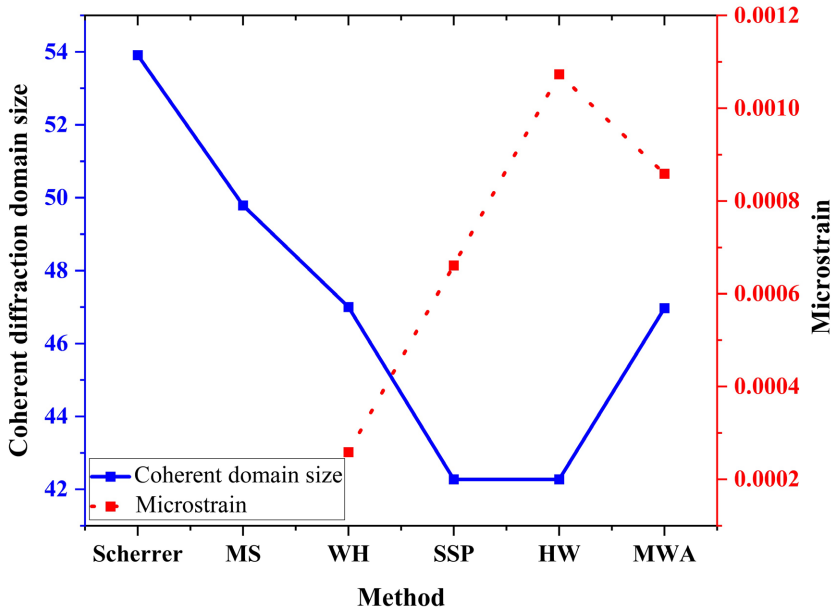

Figure 8. Evolution of microstrain as a function of the method.

Although the estimated microstrain values exhibit some dispersion, they all remain within the order of 10^{-4} - 10^{-3}, indicating overall consistency among the different analytical approaches. The Williamson-Hall (UDM) method yielded the lowest microstrain value (2.585×10^{-4}). This relatively low estimate may arise from the fundamental assumption of the model, which considers uniform and isotropic lattice deformation in all crystallographic directions. Such an assumption may not be strictly valid for porous materials such as Ce-MOF, where struc-

tural defects can lead to a heterogeneous distribution of local lattice distortions. In contrast, the Size-strain plot and Halder-Wagner methods yielded higher microstrain values of 6.614×10^{-4} and 1.073×10^{-3}, respectively. This difference mainly originates from the assumptions adopted by these methods regarding the representation of diffraction peak broadening. The size-strain plot model assumes a Lorentzian size-broadening component and a Gaussian strain-broadening component, whereas the Halder-Wagner approach employed a Voigt profile, which is often more representative of experimental diffraction peak shapes [24] [57] [58]. The microstrain value obtained using the modified Warren-Averbach method (8.587×10^{-4}) is consistent with this trend and indicates that internal lattice strain contributes to diffraction peak broadening without being its dominant source. Overall, the results obtained from the different models show good agreement while highlighting the sensitivity of peak-profile analysis to the assumptions underlying each analytical approach [57]. The positive microstrain values indicate that the coherent diffraction domains are subjected to tensile lattice strain [49] [59]. These findings indicate that the synthesized material consists of nanocrystalline domains, with the estimated size corresponding to coherent diffraction domains rather than to the physical particle size. In metal-organic frameworks, such microstrain may originate from metal-ligand coordination defects [60] [61], structural vacancies, and local lattice distortions generated during crystal nucleation and growth [5] [62]. Furthermore, the relatively small difference between the coherent diffraction domain size obtained from the Scherrer equation and those derived from strain-inclusive models suggests that the finite size of the coherent diffraction domains is the predominant contributor to diffraction peak broadening in the present Ce-MOF, whereas the contribution of lattice microstrain remains comparatively limited [57] [58]. Therefore, the microstructural parameters obtained in this study should be interpreted as estimates of coherent diffraction domain size and lattice microstrain, rather than as a definitive description of the material microstructure.

The dislocation densities estimated (**Table 2**) using the relation $\delta = 1/D^2$ (Equation (10)) [39] are on the order of 10^{14} m^{-2}. These values suggest the presence of crystallographic defects within the synthesized Ce-MOF and are consistent with the existence of local lattice distortions commonly reported in metal-organic frameworks [5]. Since the dislocation density is derived from the coherence diffraction domain size, it should be regarded as an indirect indicator of the defect density rather than a direct measurement of dislocations. Accordingly, the observed diffraction peak broadening reflects the combined effect of the finite size of coherent diffraction domains, lattice microstrain, and crystallographic defects, thereby providing averaged structural information over the diffracting volume [63]. In MOFs, such defects may originate from missing-linker or missing-cluster defects, coordination disorder, or local structure distortions and can increase the number of accessible active sites, although they may also compromise the structural stability of the framework [5].

Table 2. Estimated dislocation densities.

$\delta \times 10^{14}$ (m^{-2})					
Scherrer	MS	WH	SSP	HW	MWA
3.44	4.03	4.527	5.596	5.596	4.533

3.3. Scanning Electron Microscopy Coupled with Energy-Dispersive Spectroscopy

SEM observations (**Figure 9**) reveal aggregates of asymmetric particles with a size variation ranging from 44.65 to 199.32 µm (**Figure 10**), characterized by an irregular morphology without a well-defined crystalline shape, indicating non-uniform growth dominated by rapid nucleation. This morphology may be attributed to the presence of sulfate traces from the cerium precursor, likely to disrupt crystal growth [35] [36]. These data are consistent with those reported for MOFs synthesized by solvo/hydrothermal treatments [64] [65]. The ×100 magnification allowed the overall particle distribution to be observed, while surface details are revealed at ×500, ×1000, and ×2000 magnifications, showing microscopic relief features and surface irregularities. These structures increase the specific surface area and can generate active sites favorable for adsorption or catalysis [66]. EDS analysis confirmed the elemental composition of the synthesized MOF-type product. The spectra (**Figure 11**) show cerium (26.84% - 29.77%), carbon (7.58% - 8.34%), oxygen (46.62% - 51.29%), and sulfur (13.53% - 16.03%) contents, depending on the targeted areas.

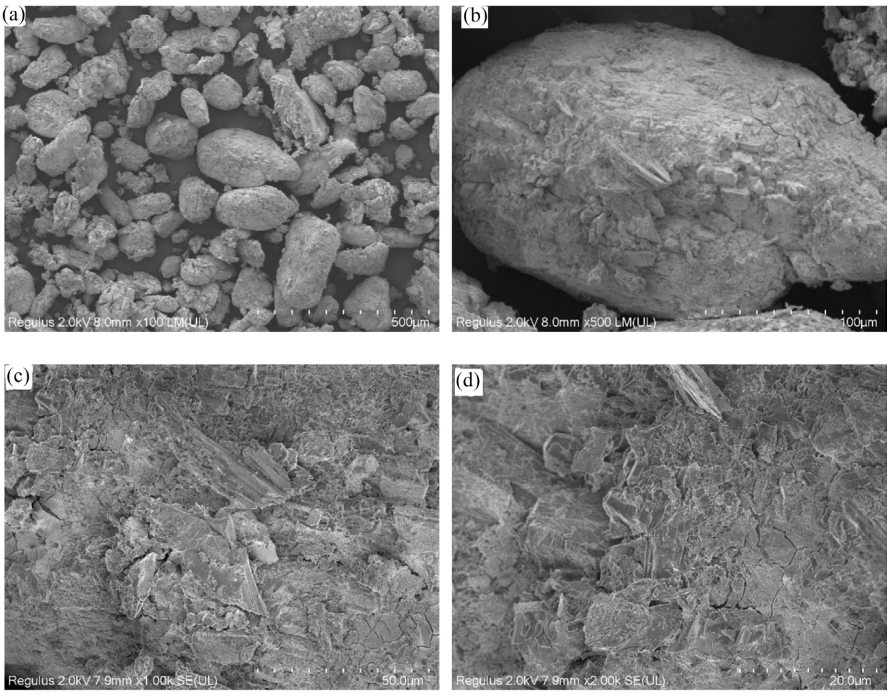

Figure 9. SEM of synthesized compound; scale (µm): (a) 500, (b) 100, (c) 50, (d) 20.

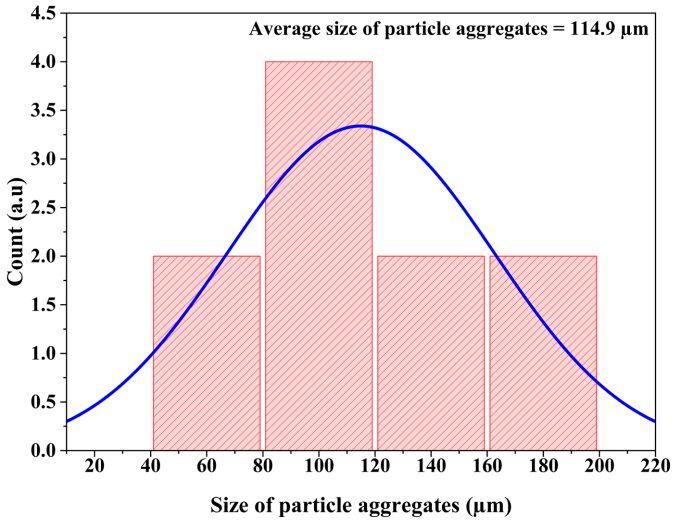

Figure 10. Aggregate size of the particles of the synthesized product.

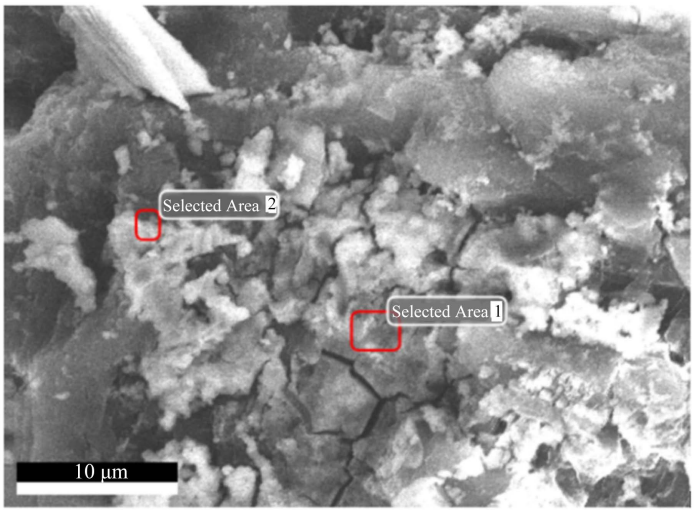

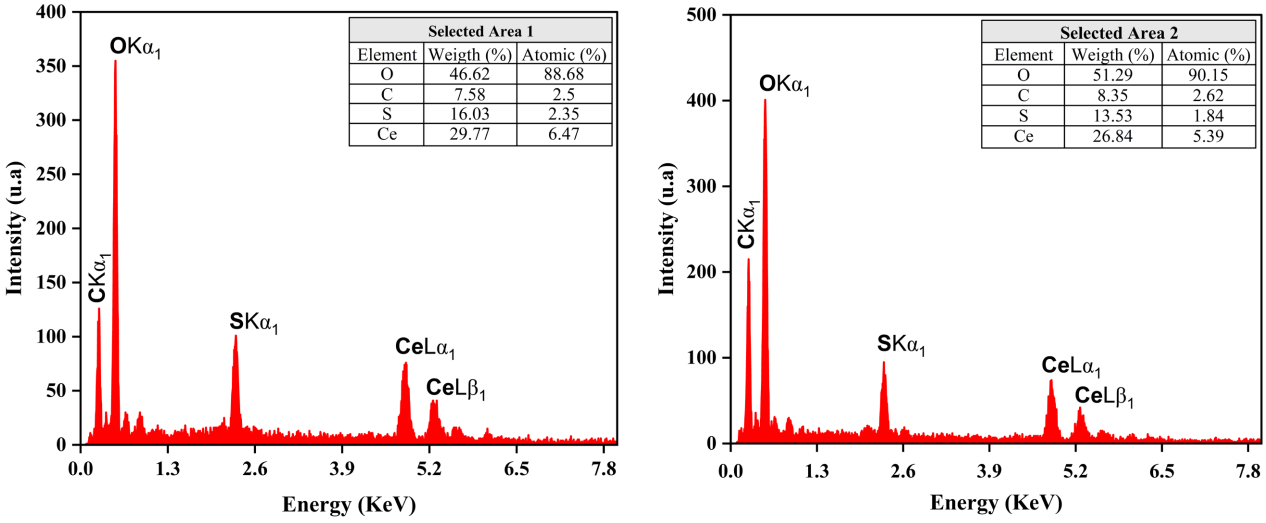

Figure 11. SEM-EDS of the synthesized compound.

3.4. Infrared

Figure 12 presents the infrared spectrum of the synthesized product. The bands located at 449 and 500 cm^{-1} are attributed to the stretching vibrations of Ce-O bonds and the O-Ce-O bending modes [67] [68]; their presence confirms the effective coordination of the ligand to cerium. The band at 725 cm^{-1} is related to the bending of a di-substituted aromatic ring. The bands at 879 and 927 cm^{-1} [69] [70] are attributed to the vibration of the para-substituted aromatic ring. The bands at 725, 879, and 927 cm^{-1} confirm the terephthalate structure. The band at 1112 cm^{-1} is attributed to the stretching vibrations of C-C bonds of the aromatic core, with a possible contribution from C-O vibrations of the carboxylate group [69] [71]. This band at 1112 cm^{-1} may also reflect the contribution of S-O stretching vibrations arising from residual sulfate. The band at 1282 cm^{-1} corresponds to the C = O vibration of the carboxylate. The bands at 1407 and 1422 cm^{-1} are associated with the symmetric stretching vibrations of COO^-, while the band at 1574 cm^{-1} corresponds to the asymmetric stretching vibration of COO^- [67] [72]-[75]. The band at 1509 cm^{-1} is related to the C = C bond of the aromatic core. The bands at 3104 and 3064 cm^{-1} are attributed to aromatic C-H bending. The broad band around 3500 cm^{-1} is associated with OH from water in the structure [67] [69] [73] [76] and is confirmed by the bands at 2814, 2656, and 2537 cm^{-1}. The coexistence of asymmetric and symmetric stretching vibrations of the carboxylates, with wavenumber difference values $\Delta\nu$ $[\nu_{asym(COO^-)} - \nu_{sym(COO^-)}]$ ranging between 152 and 167 cm^{-1}, indicates a bridging coordination mode or a mixed bridging-bidentate or chelating mode [74] [77]. The splitting of the symmetric band may indicate multiple coordination environments or structural disorder [67] [78] [79]. The experimental data show similarity with those of UiO-66 (Ce) MOF in terms of symmetric and asymmetric stretching and Ce-O bond vibrations. The band at 1674 cm^{-1} highlights the presence of protonated carboxylate groups (residual or coordinating water molecules), indicating a higher degree of structural defects or incomplete deprotonation compared to UiO-66(Ce).

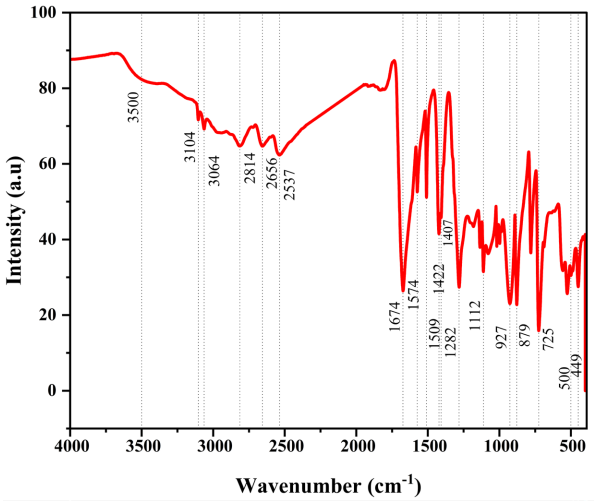

Figure 12. Infrared spectrum of the synthesized product.

3.5. X-Ray Fluorescence

Figure 13 presents the chemical composition of the synthesized compound. The data showed that this technique allowed only the metal center (Ce, Z = 58) and sulfur (Z = 16) to be identified, while the elements (C, O, H) constituting the organic ligand were not detected due to the detection limit of this technique for light elements [80]-[82]. These results revealed the dominance of cerium with a percentage of 83.4% and sulfur at 7.8%. The missing percentage of 8.9% would therefore be attributed to carbon, oxygen, and hydrogen. This analysis may be considered as a partial contribution from the inorganic part of the material, leading to an apparent overestimation of the metallic fraction. EDS and FTIR, thus validating the formation of a hybrid MOF-Ce compound, achieved the detection of C, O, and H constituting the organic ligand.

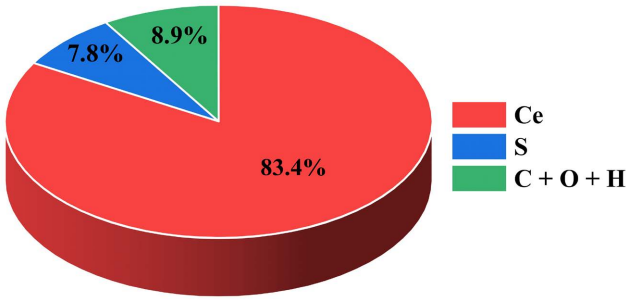

Figure 13. Chemical composition of the synthesized compound.

4. Conclusion

This study provided a comparative evaluation of the coherent diffraction domain size and lattice microstrain using the Scherrer, Monshi-Scherrer, Williamson-Hall, Size-Strain Plot, Halder-Wagner, and modified Warren-Averbach (without Fourier transform) methods. The estimated coherent diffraction domain sizes ranged from 42.27 to 53.91 nm, depending on the analytical model employed. The strain-inclusive methods yielded lattice microstrain values on the order of 10^{-4} - 10^{-3}. The close agreement between the coherent domain sizes obtained from the Size-Strain plot and Halder-Wagner methods supports the consistency of the microstructural estimations, despite the different assumptions underlying each analytical approach. SEM observations revealed aggregates of irregularly shaped particles with heterogeneous morphology, whereas FTIR spectra exhibited the characteristic vibrational bands associated with the cerium-based MOF. X-ray fluorescence and EDS analyses confirmed the elemental composition and the homogeneous distribution of the constituent elements within the synthesized material.

Acknowledgements

The authors express their gratitude to the Director General of the Geological and Mining Research Center (CRGM) of the Republic of the Congo for technical and administrative support.

Data Availability Statement

The authors confirm that data supporting the findings of this study are available within the article.

Author Contributions

Ferland Ngoro-elenga: conceptualization, data curation, methodology, writing-original draft, and writing-review and editing; Aurore Coeursa Leko: methodology; Hubert Makomo: methodology and supervision; Fernand Atipo Itoua Ngopoh: methodology, writing-review and editing; Arnaud Ottard Ossiby Mwa Ngo: writing-review; Timothée Nsongo: validation and supervision. All authors have read and approved the final version of the manuscript.

Conflicts of Interest

The authors declare that they have no conflicts of interest.

References

[1] Raptopoulou, C.P. (2021) Metal-Organic Frameworks: Synthetic Methods and Potential Applications. *Materials*, **14**, Article No. 310. https://doi.org/10.3390/ma14020310

[2] Samanidou, V.F. and Deliyanni, E.A. (2020) Metal Organic Frameworks: Synthesis and Application. *Molecules*, **25**, Article No. 960. https://doi.org/10.3390/molecules25040960

[3] Rasheed, T., Rizwan, K., Bilal, M. and Iqbal, H.M.N. (2020) Metal-Organic Framework-Based Engineered Materials—Fundamentals and Applications. *Molecules*, **25**, Article No. 1598. https://doi.org/10.3390/molecules25071598

[4] Cavalcante, L.S.R., Dettmann, M.A., Sours, T., Yang, D., Daemen, L.L., Gates, B.C., *et al.* (2023) Elucidating Correlated Defects in Metal Organic Frameworks Using Theory-Guided Inelastic Neutron Scattering Spectroscopy. *Materials Horizons*, **10**, 187-196. https://doi.org/10.1039/d2mh00914e

[5] Xiang, W., Zhang, Y., Chen, Y., Liu, C. and Tu, X. (2020) Synthesis, Characterization and Application of Defective Metal-Organic Frameworks: Current Status and Perspectives. *Journal of Materials Chemistry A*, **8**, 21526-21546. https://doi.org/10.1039/d0ta08009h

[6] Islamov, M., Boone, P., Babaei, H., McGaughey, A.J.H. and Wilmer, C.E. (2023) Correlated Missing Linker Defects Increase Thermal Conductivity in Metal-Organic Framework UiO-66. *Chemical Science*, **14**, 6592-6600. https://doi.org/10.1039/d2sc06120a

[7] Moore, S.C., Smith, M.R., Trettin, J.L., Yang, R.A. and Sarazen, M.L. (2023) Kinetic Impacts of Defect Sites in Metal-Organic Framework Catalysts under Varied Driving Forces. *ACS Energy Letters*, **8**, 1397-1407. https://doi.org/10.1021/acsenergylett.2c02893

[8] Knebel, A. and Caro, J. (2023) Metal-Organic Frameworks and Covalent Organic Frameworks as Disruptive Membrane Materials for Energy-Efficient Gas Separation. *Nature Nanotechnology*, **17**, 911-923. https://doi.org/10.1038/s41565-022-01168-3

[9] Liu, J., Li, Y. and Lou, Z. (2022) Recent Advancements in MOF/Biomass and Bio-MOF Multifunctional Materials: A Review. *Sustainability*, **14**, Article No. 5768.

https://doi.org/10.3390/su14105768

[10] Hai, G. and Wang, H. (2022) Theoretical Studies of Metal-Organic Frameworks: Calculation Methods and Applications in Catalysis, Gas Separation, and Energy Storage. *Coordination Chemistry Reviews*, **469**, Article ID: 214670. https://doi.org/10.1016/j.ccr.2022.214670

[11] Finelli, V., Rojas-Buzo, S., Signorile, M., Bonino, F. and Bordiga, S. (2025) Exploring Ce(IV)-MOFs Redox Behavior for Catalysis by Spectroscopies. *Nano Materials Science*, **7**, 761-772. https://doi.org/10.1016/j.nanoms.2024.11.001

[12] Wang, X., Reischauer, S., Xie, H., Han, G., Wellman, H., Kirlikovali, K.O., *et al.* (2024) Advancements in Cerium/Titanium Metal-Organic Frameworks: Unparalleled Stability in CO Oxidation. *Matter*, **7**, 3845-3856. https://doi.org/10.1016/j.matt.2024.07.013

[13] Wang, P., Wang, F., Liu, Q., Zhang, Y., Le, S. and Zhu, C. (2025) Application of Ceria Materials Modified by Oxygen Vacancies: In Photocatalytic Process. *Journal of Rare Earths*, **43**, 417-429. https://doi.org/10.1016/j.jre.2024.03.022

[14] Jacobsen, J., Ienco, A., D'Amato, R., Costantino, F. and Stock, N. (2020) The Chemistry of Ce-Based Metal-organic Frameworks. *Dalton Transactions*, **49**, 16551-16586. https://doi.org/10.1039/d0dt02813d

[15] Othman, A., Gowda, A., Andreescu, D., Hassan, M.H., Babu, S.V., Seo, J., *et al.* (2024) Two Decades of Ceria Nanoparticle Research: Structure, Properties and Emerging Applications. *Materials Horizons*, **11**, 3213-3266. https://doi.org/10.1039/d4mh00055b

[16] Tian, J., Zhong, J., Xie, Z., Cai, H., Song, L., Lei, K., *et al.* (2026) Activating Lattice Oxygen via Self-Adaptive Ce^{4+}-O-Ce^{3+} Symmetry-Breaking Sites in Ceria for Volatile Organic Compounds Oxidation. *Applied Catalysis B: Environment and Energy*, **385**, Article ID: 126307. https://doi.org/10.1016/j.apcatb.2025.126307

[17] De Souto Neto, A.L., Raimundo, R.A., Da Silva Hortêncio, J., De Oliveira, A.L.M., Da Silva, R.B., Da Silva, J.I.G., *et al.* (2026) Engineering Metal-Organic Frameworks Precursors and Thermal Treatment to Achieve High-Activity CeO_2 Oxygen Evolution Electrocatalysts. *Colloids and Surfaces A: Physicochemical and Engineering Aspects*, **742**, Article ID: 140495. https://doi.org/10.1016/j.colsurfa.2026.140495

[18] Baweja, R., Verma, M., Gautam, S., Upreti, S. and Goyal, N. (2024) Enhanced Electrochemical Performance of Ce-MOF/h-CeO_2 Composites for High-Capacitance Energy Storage Applications. *RSC Advances*, **14**, 17855-17865. https://doi.org/10.1039/d4ra00523f

[19] Rojas-Buzo, S., Salusso, D., Le, T.T., Ortuño, M.A., Lomachenko, K.A. and Bordiga, S. (2024) Unveiling the Role and Stabilization Mechanism of Cu^{2+} into Defective Ce-MOF Clusters during CO Oxidation. *The Journal of Physical Chemistry Letters*, **15**, 3962-3967. https://doi.org/10.1021/acs.jpclett.4c00324

[20] Yu, J., Wu, Y., Peng, T., Qi, Q., Ma, X., Gu, Y., *et al.* (2024) Controllable Amorphization and Morphology Engineering on Mixed-Valence MOFs for Ultra-Fast and High-Stability Near-Pseudocapacitance Li^+ Storage. *Chemical Communications*, **60**, 10898-10901. https://doi.org/10.1039/d4cc02692f

[21] Zorlu, T., Hetey, D., Reithofer, M.R. and Chin, J.M. (2024) Physicochemical Methods for the Structuring and Assembly of MOF Crystals. *Accounts of Chemical Research*, **57**, 2105-2116. https://doi.org/10.1021/acs.accounts.4c00250

[22] Zhang, W., Wang, Y., Wang, L., Li, Y., Sun, H., Liu, C., *et al.* (2025) Structural Functionalization of TEMPO Modified Ni-MOF for Electrocatalytic Applications. *Scientific Reports*, **15**, Article No. 42694. https://doi.org/10.1038/s41598-025-26863-8

[23] Nikmehr, S., Kazemzad, M., Sabzehmeidani, M.M., Nikzad, L. and Ebadzadeh, T. (2024) Structural Characteristics of Zn-MOFs and Derived Zinc Oxide by X-Ray Diffraction Peak Analysis Fabricated by Mechanical and Hydrothermal Methods. *Open-Nano*, **16**, Article ID: 100203. https://doi.org/10.1016/j.onano.2024.100203

[24] Madansure, Y.S., Gurav, S.K., Balsure, S.D., Gaikwad, P.K., Imran, A., El-Toni, A.M., *et al.* (2026) X-Ray Diffraction Analysis by Williamson-Hall, Strain-Size, Halder-Wagner, and Nelson-Riley Methods, and Its Co-Relationship with Elastic and Magnetic Properties of Ce^{3+} Substituted Fe-Rich Cobalt Ferrite. *Journal of Materials Science: Materials in Electronics*, **37**, Article No. 706. https://doi.org/10.1007/s10854-026-17126-x

[25] Neethu, R.P. and Madhu, G. (2025) Temperature and Defect-Induced Modulation of AC Conductivity and Dielectric Behaviour in Nickel Oxide Nanoparticles. *Discover Materials*, **5**, Article No. 117. https://doi.org/10.1007/s43939-025-00299-3

[26] Stanisławska, A., Seramak, T., Zasińska, K., Gaweł, Ł., Gajowiec, G., Gazda, M., *et al.* (2025) Influence of Laser Powder Bed Fusion Build Orientation on the Corrosion Resistance of CoCrWMo Alloy Considering Dislocation Density Character and Lattice Microstrain. *Scientific Reports*, **15**, Article No. 45625. https://doi.org/10.1038/s41598-025-30143-w

[27] Madisetti, D., Sudmanns, M., Stiles, C.D. and El-Awady, J.A. (2025) Computational Investigation into XRD Peak Broadening Effects with Discrete Dislocation Dynamics in Additively Manufactured 316L Stainless Steel. *Journal of the Mechanics and Physics of Solids*, **196**, Article ID: 105970. https://doi.org/10.1016/j.jmps.2024.105970

[28] Belaye, M., Taddesse, A.M., Teju, E., Sanchez-Sanchez, M. and Yassin, J.M. (2023) Preparation and Adsorption Behavior of Ce(III)-MOF for Phosphate and Fluoride Ion Removal from Aqueous Solutions. *ACS Omega*, **8**, 23860-23869. https://doi.org/10.1021/acsomega.3c02290

[29] Maiti, S., Dhawa, T., Mallik, A.K. and Mahanty, S. (2017) CeO_2@C Derived from Benzene Carboxylate Bridged Metal-Organic Frameworks: Ligand Induced Morphology Evolution and Influence on the Electrochemical Properties as a Lithium-Ion Battery Anode. *Sustainable Energy & Fuels*, **1**, 288-298. https://doi.org/10.1039/c6se00026f

[30] Molavi, H., Saeedi, S. and Ghorbani, A. (2026) Green Synthesis of Amorphous Ce-MOFs as Efficient Adsorbents Towards Ofloxacin Antibiotics. *Scientific Reports*, **16**, Article No. 11322. https://doi.org/10.1038/s41598-026-42188-6

[31] Tang, T., Jin, X., Tao, X., Huang, L. and Shang, S. (2022) Low-Crystalline Ce-Based Bimetallic MOFs Synthesized via DBD Plasma for Excellent Visible Photocatalytic Performance. *Journal of Alloys and Compounds*, **895**, Article ID: 162452. https://doi.org/10.1016/j.jallcom.2021.162452

[32] Feng, Y., Wu, J.-X., Mo, Y.-H., Liu, S., Cai, S.-L., Zhang, W.-G., *et al.* (2024) Hierarchical Porous Amorphous Metal-organic Frameworks Constructed from ZnO/MOF Glass Composites. *Chemical Communications*, **60**, 6190-6193. https://doi.org/10.1039/d4cc01454e

[33] Abid, H.R., Azhar, M.R., Iglauer, S., Rada, Z.H., Al-Yaseri, A. and Keshavarz, A. (2024) Physicochemical Characterization of Metal Organic Framework Materials: A Mini Review. *Heliyon*, **10**, e23840. https://doi.org/10.1016/j.heliyon.2023.e23840

[34] Xu, D., Cao, X., Zhou, J., Lin, Z., Wang, J., Han, J., *et al.* (2025) Analysis of Microstructure Properties of Ni-Fe MOFs and Their Influence on Selective Recognition of Single and Binary Dye Systems. *NPJ Clean Water*, **8**, Article No. 35. https://doi.org/10.1038/s41545-025-00470-6

[35] Grebenyuk, D., Shaulskaya, M., Shevchenko, A., Zobel, M., Tedeeva, M., Kustov, A., *et al*. (2023) Tuning the Cerium-Based Metal-Organic Framework Formation by Template Effect and Precursor Selection. *ACS Omega*, **8**, 48394-48404. https://doi.org/10.1021/acsomega.3c07906

[36] Yang, S., Wang, Q., Zhao, H. and Liu, D. (2022) Bottom-Up Synthesis of MOF-Derived Magnetic Fe-Ce Bimetal Oxide with Ultrahigh Phosphate Adsorption Performance. *Chemical Engineering Journal*, **448**, Article ID: 137627. https://doi.org/10.1016/j.cej.2022.137627

[37] Kamran, M. and Anis-ur-Rehman, M. (2020) Enhanced Transport Properties in Ce Doped Cobalt Ferrites Nanoparticles for Resistive RAM Applications. *Journal of Alloys and Compounds*, **822**, Article ID: 153583. https://doi.org/10.1016/j.jallcom.2019.153583

[38] Kawsar, M., Hossain, M.S., Bahadur, N.M. and Ahmed, S. (2024) Synthesis of Nano-Crystallite Hydroxyapatites in Different Media and a Comparative Study for Estimation of Crystallite Size Using Scherrer Method, Halder-Wagner Method Size-Strain Plot, and Williamson-Hall Model. *Heliyon*, **10**, e25347. https://doi.org/10.1016/j.heliyon.2024.e25347

[39] Azad, M.A.S., Hossain, M.S., Saikat, S.P., Hasan, M.R. and Bhowmik, S. (2025) Structural Insights into Zinc Oxide-Silver Nanocomposite *via* Different XRD Models: Rapid Synthesis with Photocatalytic & Antibacterial Applications. *Nanoscale Advances*, **7**, 8138-8153. https://doi.org/10.1039/d5na00790a

[40] Disha, S.A., Sahadat Hossain, M., Habib, M.L. and Ahmed, S. (2024) Calculation of Crystallite Sizes of Pure and Metals Doped Hydroxyapatite Engaging Scherrer Method, Halder-Wagner Method, Williamson-Hall Model, and Size-Strain Plot. *Results in Materials*, **21**, Article ID: 100496. https://doi.org/10.1016/j.rinma.2023.100496

[41] Nath, D., Singh, F. and Das, R. (2020) X-Ray Diffraction Analysis by Williamson-Hall, Halder-Wagner and Size-Strain Plot Methods of CdSe Nanoparticles—A Comparative Study. *Materials Chemistry and Physics*, **239**, Article ID: 122021. https://doi.org/10.1016/j.matchemphys.2019.122021

[42] Jannat, M.R., Biswas, B., Rahman, M.L., Ahmed, M.F., Hossain, M.J., Khanam, J., *et al*. (2025) Validity of Crystallite Size Determination Methods Based on XRD Peak Broadening in Pure and Metal-Doped Nickel Ferrites. *Results in Materials*, **28**, Article ID: 100762. https://doi.org/10.1016/j.rinma.2025.100762

[43] Gohr, M.S., Ali, H., Gad, S., Soliman, H.M.A. and Giba, A.E. (2026) Preparation and Characterization of Holmium Doped ZIF-8 Nanocrystals for White Light Emitting Phosphors. *Scientific Reports*, **16**, Article No. 4116. https://doi.org/10.1038/s41598-025-33503-8

[44] Sen, S.K., Hossain, M.S., Roy, R., Alam, M.S., Manir, M.S. and Biswas, G.G. (2024) Size-strain Distribution Analysis from XRD Peak Profile of (Mg, Fe) Co-Doped SnO_2 Nanoparticles Fabricated Using Chemical Co-Precipitation Route. *Ceramics International*, **50**, 44038-44055. https://doi.org/10.1016/j.ceramint.2024.08.254

[45] Hossain, M.S., Hossain, M.S., Ahmed, S. and Bin Mobarak, M. (2024) Characterization and Adsorption Performance of Nano-Hydroxyapatite Synthesized from *Conus litteratus* Waste Seashells for Congo Red Dye Removal. *RSC Advances*, **14**, 38560-38577. https://doi.org/10.1039/d4ra07733d

[46] Sedaghati-Jamalabad, G. and Bagheri-Mohagheghi, M.M. (2024) Influence of Synthesis Route on Structural Properties of $SnFe_2O_4$ Spinel Phase via Methods of Co-Precipitation, Sol-Gel and Solvothermal: Morphology, Phase Analysis, Crystallite

Size and Lattice Strain. *Discover Applied Sciences*, **6**, Article No. 202. https://doi.org/10.1007/s42452-024-05873-7

[47] Daulay, A., Andriayani, Marpongahtun and Gea, S. (2022) Synthesis Si Nanoparticles from Rice Husk as Material Active Electrode on Secondary Cell Battery with X-Ray Diffraction Analysis. *South African Journal of Chemical Engineering*, **42**, 32-41. https://doi.org/10.1016/j.sajce.2022.07.004

[48] Halder, N.C. and Wagner, C.N.J. (1966) Separation of Particle Size and Lattice Strain in Integral Breadth Measurements. *Acta Crystallographica*, **20**, 312-313. https://doi.org/10.1107/s0365110x66000628

[49] Mahn, D.H., Nha, T.T.N., Phong, L.T.H., Nam, P.H., Thanh, T.D. and Phong, P.T. (2023) Determination of the Crystalline Size of Hexagonal $La_{1-x}Sr_xMnO_3$ (x = 0.3) Nanoparticles from X-Ray Diffraction—A Comparative Study. *RSC Advances*, **13**, 25007-25017. https://doi.org/10.1039/d3ra04018f

[50] Deb, A.K. and Chatterjee, P. (2019) Estimation of Lattice Strain in Alumina-Zirconia Nanocomposites by X-Ray Diffraction Peak Profile Analysis. *Journal of Theoretical and Applied Physics*, **13**, 221-229. https://doi.org/10.1007/s40094-019-0338-z

[51] Morán, M., Álvarez, M.V., Vizcaíno, P., Brown, D.W. and Santisteban, J. (2022) Dislocation Density Evolution in Cold-Rolled Zr-2.5% Nb Pressure Tubes under Thermal Treatments by High Energy XRD and Neutron TOF Diffraction Peak Profile Analysis. *Journal of Alloys and Compounds*, **929**, Article ID: 167196. https://doi.org/10.1016/j.jallcom.2022.167196

[52] Cho, C.-H., Son, K. and Cho, H. (2023) Experimental Analysis of Deformation Texture Evolutions in Pure Cu, Cu-37Zn, Cu-6Mg and -8Mg Alloys at Cold-Rolling Processes. *Journal of Alloys and Compounds*, **934**, Article ID: 167879. https://doi.org/10.1016/j.jallcom.2022.167879

[53] Cho, C.-H., Lee, J.-W., Son, K.-T. and Hyum, S.-K. (2021) Strain Rate Effects on Microstructure and Texture Evolution in Cold-Sheared Al-6Mg Alloys during Low-Temperature Annealing. *Journal of Alloys and Compounds*, **889**, Article ID: 161630. https://doi.org/10.1016/j.jallcom.2021.161630

[54] Youssef, K.M., Scattergood, R.O., Murty, K.L. and Koch, C.C. (2006) Nanocrystalline Al-Mg Alloy with Ultrahigh Strength and Good Ductility. *Scripta Materialia*, **54**, 251-256. https://doi.org/10.1016/j.scriptamat.2005.09.028

[55] El-Makaty, F.M., Andre Mkhoyan, K. and Youssef, K.M. (2021) The Effects of Structural Integrity of Graphene on the Thermoelectric Properties of the N-Type Bismuth-Telluride Alloy. *Journal of Alloys and Compounds*, **876**, Article ID: 160198. https://doi.org/10.1016/j.jallcom.2021.160198

[56] Hassanzadeh-Tabrizi, S.A. (2023) Precise Calculation of Crystallite Size of Nanomaterials: A Review. *Journal of Alloys and Compounds*, **968**, Article ID: 171914. https://doi.org/10.1016/j.jallcom.2023.171914

[57] Himabindu, B., Latha Devi, N.S.M.P. and Rajini Kanth, B. (2021) Microstructural Parameters from X-Ray Peak Profile Analysis by Williamson-Hall Models; a Review. *Materials Today: Proceedings*, **47**, 4891-4896. https://doi.org/10.1016/j.matpr.2021.06.256

[58] Alam, M.K., Hossain, M.S., Bahadur, N.M. and Ahmed, S. (2024) A Comparative Study in Estimating of Crystallite Sizes of Synthesized and Natural Hydroxyapatites Using Scherrer Method, Williamson-Hall Model, Size-Strain Plot and Halder-Wagner Method. *Journal of Molecular Structure*, **1306**, Article ID: 137820. https://doi.org/10.1016/j.molstruc.2024.137820

[59] Rabiei, M., Palevicius, A., Monshi, A., Nasiri, S., Vilkauskas, A. and Janusas, G. (2020) Comparing Methods for Calculating Nano Crystal Size of Natural Hydroxyapatite Using X-Ray Diffraction. *Nanomaterials*, **10**, Article No. 1627. https://doi.org/10.3390/nano10091627

[60] An, D., Chen, L., Liang, Y., Hou, J. and Chen, J. (2024) Defect-Containing Metal-organic Framework Materials for Sensor Applications. *Journal of Materials Chemistry A*, **12**, 38-58. https://doi.org/10.1039/d3ta05592b

[61] Möslein, A.F., Donà, L., Civalleri, B. and Tan, J.-C. (2024) Defect Engineering in Metal-Organic Framework Nanocrystals: Implications for Mechanical Properties and Performance. *ACS Applied Nano Materials*, **5**, 6398-6409. https://doi.org/10.1021/acsanm.2c00493

[62] Wang, J., Liu, L., Chen, C., Dong, X., Wang, Q., Alfilfil, L., *et al.* (2020) Engineering Effective Structural Defects of Metal-Organic Frameworks to Enhance Their Catalytic Performances. *Journal of Materials Chemistry A*, **8**, 4464-4472. https://doi.org/10.1039/c9ta12230c

[63] Liu, L., Zhang, D., Zhu, Y. and Han, Y. (2020) Bulk and Local Structures of Metal-organic Frameworks Unravelled by High-Resolution Electron Microscopy. *Communications Chemistry*, **3**, Article No. 99. https://doi.org/10.1038/s42004-020-00361-6

[64] Sun, J., Yu, X., Zhao, S., Chen, H., Tao, K. and Han, L. (2020) Solvent-Controlled Morphology of Amino-Functionalized Bimetal Metal-Organic Frameworks for Asymmetric Supercapacitors. *Inorganic Chemistry*, **59**, 11385-11395. https://doi.org/10.1021/acs.inorgchem.0c01157

[65] Suresh, K., Kalenak, A.P., Sotuyo, A. and Matzger, A.J. (2022) Metal-Organic Framework (MOF) Morphology Control by Design. *Chemistry—A European Journal*, **28**, e202200334. https://doi.org/10.1002/chem.202200334

[66] Salusso, D., Mauri, S., Deplano, G., Torelli, P., Bordiga, S. and Rojas-Buzo, S. (2023) MOF-Derived CeO_2 and $CeZrO_x$ Solid Solutions: Exploring Ce Reduction through FTIR and NEXAFS Spectroscopy. *Nanomaterials*, **13**, Article No. 272. https://doi.org/10.3390/nano13020272

[67] Ismail, K.M., Rashidi, F.B. and Hassan, S.S. (2024) Ultrasonic Synthesis, Characterization, DFT and Molecular Docking of a Biocompatible Zn-Based MOF as a Potential Antimicrobial, Anti-Inflammatory and Antitumor Agent. *Scientific Reports*, **14**, Article No. 21989. https://doi.org/10.1038/s41598-024-71609-7

[68] Durmus, Z., Köferstein, R., Lindenberg, T., Lehmann, F., Hinderberger, D. and Maijenburg, A.W. (2023) Preparation and Characterization of Ce-MOF/g-C_3N_4 Composites and Evaluation of Their Photocatalytic Performance. *Ceramics International*, **49**, 24428-24441. https://doi.org/10.1016/j.ceramint.2023.01.063

[69] Abo El-Yazeed, W.S., El-Reash, Y.G.A., Elatwy, L.A. and Ahmed, A.I. (2020) Facile Fabrication of Bimetallic Fe-Mg MOF for the Synthesis of Xanthenes and Removal of Heavy Metal Ions. *RSC Advances*, **10**, 9693-9703. https://doi.org/10.1039/c9ra10300g

[70] Tabassum, S., Akter, S., Ahmed, M.F., Islam, D., Ahmed, S. and Sahadat Hossain, M. (2025) Sustainable Synthesis of Metal-Organic Frameworks from Waste Material for Electrochemical Sensing of Heavy Metal Ions in Aqueous Media. *ACS Sustainable Resource Management*, **3**, 125-136. https://doi.org/10.1021/acssusresmgt.5c00428

[71] Suo, Q., Zi, J., Bai, Z. and Qi, S. (2017) The Glycolysis of Poly(ethylene terephthalate) Promoted by Metal Organic Framework (MOF) Catalysts. *Catalysis Letters*, **147**, 240-252. https://doi.org/10.1007/s10562-016-1897-0

[72] Wei, X., Ji, T., Zhang, S., Xue, Z., Lou, C., Zhang, M., *et al.* (2022) Cerium-Terephthalic Acid Metal-Organic Frameworks for Ratiometric Fluorescence Detecting and

Scavenging·OH from Fuel Combustion Gas. *Journal of Hazardous Materials*, **439**, Article ID: 129603. https://doi.org/10.1016/j.jhazmat.2022.129603

[73] Shahabinejad, H., Binazadeh, M., Esmaeilzadeh, F., Hashemi, F. and Mousavi, S.M. (2024) Optimization of Cerium-Based Metal-Organic Framework Synthesis for Maximal Sonophotocatalytic Tetracycline Degradation. *Scientific Reports*, **14**, Article No. 16887. https://doi.org/10.1038/s41598-024-67676-5

[74] Bondarenko, L., Baimuratova, R., Reindl, M., Zach, V., Dzeranov, A., Pankratov, D., *et al.* (2024) Dramatic Change in the Properties of Magnetite-Modified MOF Particles Depending on the Synthesis Approach. *Heliyon*, **10**, e27640. https://doi.org/10.1016/j.heliyon.2024.e27640

[75] Rego, R.M., Sriram, G., Ajeya, K.V., Jung, H.-Y., Kurkuri, M.D. and Kigga, M. (2021) Cerium Based UiO-66 MOF as a Multipollutant Adsorbent for Universal Water Purification. *Journal of Hazardous Materials*, **416**, Article ID: 125941. https://doi.org/10.1016/j.jhazmat.2021.125941

[76] Butova, V., Drenchev, N.L. and Hadjiivanov, K.I. (2026) *In Situ* FTIR Investigation of Metal Node Chemistry in Zr-, Ce-, and Zr-Ce Bimetallic UiO-66 Frameworks. *Precision Chemistry*, **4**, 1062-1069. https://doi.org/10.1021/prechem.5c00436

[77] Yuan, F., Yuan, C., Cao, B., Di, Y., Wang, S., Liu, M., *et al.* (2020) Two Ln-Based Metal-Organic Frameworks Based on the 5-(1H-1,2,4-triazol-1-yl)-1,3-benzenedicarboxylic Acid Ligand: Syntheses, Structures, and Photocatalytic Properties. *RSC Advances*, **10**, 39771-39778. https://doi.org/10.1039/d0ra07159e

[78] Hadjiivanov, K.I., Panayotov, D.A., Mihaylov, M.Y., Ivanova, E.Z., Chakarova, K.K., Andonova, S.M., *et al.* (2021) Power of Infrared and Raman Spectroscopies to Characterize Metal-Organic Frameworks and Investigate Their Interaction with Guest Molecules. *Chemical Reviews*, **121**, 1286-1424. https://doi.org/10.1021/acs.chemrev.0c00487

[79] Capková, D., Kazda, T., Králý, N., Volavka, D., Obšatník, P., Šimek, A., *et al.* (2025) MOF-74(M) (M = Mg(II), Fe(II), Ni(II)) Frameworks to Enable Accelerated Redox Kinetics for Li-S Batteries. *Scientific Reports*, **15**, Article No. 38396. https://doi.org/10.1038/s41598-025-22340-4

[80] Heimler, K., Gottschalk, C. and Vogt, C. (2023) Confocal Micro X-Ray Fluorescence Analysis for the Non-Destructive Investigation of Structured and Inhomogeneous Samples. *Analytical and Bioanalytical Chemistry*, **415**, 5083-5100. https://doi.org/10.1007/s00216-023-04829-x

[81] Ravansari, R., Wilson, S.C. and Tighe, M. (2020) Portable X-Ray Fluorescence for Environmental Assessment of Soils: Not Just a Point and Shoot Method. *Environment International*, **134**, Article ID: 105250. https://doi.org/10.1016/j.envint.2019.105250

[82] López-Núñez, R. (2022) Portable X-Ray Fluorescence Analysis of Organic Amendments: A Review. *Applied Sciences*, **12**, Article No. 6944. https://doi.org/10.3390/app12146944